

Article

# A Survey of African Weather and Climate Extremes

Mark R. Jury <sup>1,2</sup> 

<sup>1</sup> Geography Department, University of Zululand, KwaDlangezwa, Empangeni 3886, South Africa; mark.jury@upr.edu

<sup>2</sup> Physics Department, University of Puerto Rico Mayagüez, Mayaguez, PR 00681, USA

**Abstract:** A survey of African weather and climate extremes in the period 1970–2023 reveals spatial and temporal patterns of intense dry and wet spells, associated with meteorological conditions and consequences. Seasonal wind storms occur along coasts facing the Mozambique Channel, the Gulf of Guinea, the Mediterranean, and the Southern Ocean. Desiccating evaporation is found along the edge of the Sahara and Kalahari Deserts, as well as in lowland subtropical river valleys. The Palmer Drought Severity Index (PDSI) and net outgoing longwave radiation (OLR) reflect precipitation–evaporation balance and guide regional evaluation. Temporal fluctuations are dominated by inter-decadal oscillations and drying/moistening trends over Southeast/West Africa, respectively. Localized floods and droughts are frequent, but widespread impacts are rare, suggesting that the transfer of resources from surplus to deficit regions is possible. Various case studies focus on (i) tropical cyclone impacts, (ii) monsoon moisture flux, and (iii) coastal upwelling. African communities have become resilient in the face of extreme weather and have shown that adaptation is possible, but further mitigating efforts are needed so that macro-economic progress does not come with harmful secondary consequences.

**Keywords:** Africa; extreme weather; climate variability and trends



**Citation:** Jury, M.R. A Survey of African Weather and Climate Extremes. *Climate* **2024**, *12*, 65. <https://doi.org/10.3390/cli12050065>

Academic Editor: Timothy G. F. Kittel

Received: 29 October 2023

Revised: 26 April 2024

Accepted: 1 May 2024

Published: 5 May 2024



**Copyright:** © 2024 by the author. Licensee MDPI, Basel, Switzerland. This article is an open access article distributed under the terms and conditions of the Creative Commons Attribution (CC BY) license (<https://creativecommons.org/licenses/by/4.0/>).

## 1. Introduction

Large swings in the African climate are a part of life on this continent. Whether floods or drought, affecting urban infrastructure or rural ecosystems, communities exposed to extreme weather become nomadic or resilient. Research on this topic includes sub-regional maximum daily rainfall trends from gauges and model simulations [1]. However, few continent-wide surveys have been made using high-resolution hindcast reanalyses that bring together station and satellite measurements. This gap in the research can be filled, to aid in disaster management that prioritizes the use of limited resources.

Africa is poised to diversify its macro-economic efforts from agriculture and commodity extraction to industrial manufacturing and service provision [2]. Africa's 1.4 B population is relatively dispersed and growing at ~3% per annum. Food production has kept pace and per capita income has doubled since 1970—adjusted for inflation [3]. However, one-third of Africa is covered by sub-tropical deserts that release clouds of dust, and human encroachment on tropical forests generates smoke plumes that alter global radiation budgets. Although numerous rivers flow out of tropical Africa, sub-tropical water resources are stressed by evaporation—water demand exceeds supply, challenging adaptive strategies [4].

The authors of [5] describe Africa as being vulnerable to extreme weather events, because of floods and their hydrological impacts [6]. The study in [7] reports an upward trends for daily rainfall in many parts of Africa, but uncertainty arises due to its uneven monitoring [8,9]. After decades of drought, recent analyses have found an increase in the frequency of mesoscale convective systems [10,11] amidst steady seasonal rainfall totals [12] that reflect the parallel influences of climate variability and global warming [13,14]. In some regions, downward trends in the number of wet days have emerged [15–18] that

may be the forerunner of water scarcity, yet multi-year climate anomalies tend to exceed long-term trends due to localized dry and wet spells.

Seasonal climate forecasts have been used for strategic planning around the El Niño Southern Oscillation (ENSO), a multi-year zonal tilting of tropical thermoclines and atmospheric circulations that push and pull moist convection across ocean basins [19–22]. Although prediction holds value for many communities, the ENSO’s forcing of African climate exhibits decadal instability and seasonal decoupling [23]. At longer time-scales there is a poleward expansion of tropical monsoons coupled to an accelerating Hadley Cell [24].

Here, evidence of extreme weather and climate across Africa is surveyed for spatial structure and meteorological features. Employing modern high-resolution reanalysis that incorporates satellite measurements since the 1970s will generate valuable knowledge and understanding that leads to improved strategic planning for sustainable development. A key question is whether long-term temporal records of extreme daily rainfall and wind, as well as monthly evaporation and temperature, exhibit significant upward trends that make communities more vulnerable. Inferences therefore assume that the past few decades reflect a changing climate that will persist over the next few decades.

This survey gathers data on short- and long-term weather events across Africa and compiles the information into an atlas by parameter, location, and date. The following section covers the datasets and statistical methods, followed by the outcomes on climatology and annual cycles, intra-seasonal and inter-annual fluctuations, spatial patterns of daily and monthly extremes, analysis of extreme events, and long-term trends in observed and model-simulated daily and monthly extremes. This survey begins with an all-Africa spatial analysis of average and extreme weather, proceeds to characterize regional temporal fluctuations, and uncovers local drivers of extreme climate, via case studies. The goal is to determine the location and intensity of extremes, then to isolate the timing and trends of extremes at daily to multi-annual timescales within objectively defined regions.

## 2. Data and Methods

Socio-economic indices were obtained through the FAO on per capita income, adjusted for inflation and total agricultural production. Meteorological conditions were described by European Reanalysis v5 (ERA5) [25] at 25 km resolution in the period 1970–2022. ERA5 has consistently assimilated African weather data over many decades and uses satellite measurements and model physics to fill in the sparse monitoring network (Figure A1). Daily field data include rainfall, temperature, wind velocity, vertical motion (omega), and boundary layer height. Indicators of gains and losses in the water balance include the daily NOAA interpolated satellite net outgoing longwave radiation (net OLR) [26] and the monthly station-based CRU v4 Palmer Drought Severity Index (PDSI), calculated as precipitation minus potential evaporation [27,28]. Land surface conditions were analyzed via NOAA satellite surface temperature and vegetation color fraction [29,30]. Drought was characterized by monthly ERA5 potential evaporation, subsidence at 500 hPa, and air temperature. Rainfall characteristics were studied via multi-satellite interpolated CPC morphed (cMorph) and Global precipitation monitoring (GPM) products [31] and daily ERA5 (GloFAS) river discharge [32] at 25 km resolution. Long-term averages were calculated for many parameters to acquaint the reader with Africa’s circulation, convection, heat flux, and air chemistry. Table 1 lists the dataset acronyms and details.

**Table 1.** Dataset acronyms and details.

Acronym	Name (Variables)	Resolution
CLOUDSAT	Satellite microwave radar (cloud reflectivity)	10 km
cMorph GPM	Multi-satellite interpolated infrared + microwave radiance (rainfall)	25 km

Table 1. Cont.

Acronym	Name (Variables)	Resolution
CRU4	Climate Research Unit v4 (station Palmer Drought Severity Index)	50 km
EC	European Community (GloFAS river discharge)	25 km
ERA5	European Reanalysis v5 (humidity, omega, pot. evap., rain, temp, wind)	25 km
EVI	Enhanced Vegetation Index (satellite color fraction)	10 km
FAO	Food and Agricultural Organization (socio-economic data)	Country-level
HADLEY	Hadley Centre earth system model coupled ensemble simulation	150 km
MERRA2	Meteorological Reanalysis v2 NASA (air chemistry)	50 km
NOAA	Nat. Ocean Atmos. Admin. (SST, land temp, tropical cyclones)	25 km
net OLR	Satellite net outgoing longwave radiation	100 km
SODA	Simple Ocean Data Assimilation (currents, salinity, sea temp)	50 km

A useful indicator of warm, dry spells is potential evaporation. It is derived from the Penman–Monteith formula for station data and from sensible heat flux for model data. It represents the turbulent demand for surface moisture and can be measured via A-pan. Potential evaporation should be distinguished from actual evapo-transpiration, derived from latent heat flux. PDSI is based on precipitation minus potential evaporation (P–E).

Our geographic focus is 36S–38N, 20W–55E—continental Africa. Adjacent marine conditions are analyzed via NOAA satellite sea surface temperature (SST) at 25 km resolution. The air chemistry over Africa is studied via MERRA2 [33] assimilated surface dust and carbon monoxide concentrations, underpinned by satellite measurements. The period of record varies according to measurement technology and data integrity—monthly CRU4 PDSI and ERA5 rainfall and potential evaporation, 1970+; infrared and visible satellite products and wind, 1980+; and microwave (MW) satellite rainfall and air chemistry, 2000+. All products were evaluated up to 2023. The record length is 16250 days for net OLR 1979–2023 and 19,540 days for rainfall and temperature from 1970 to 2023.

Extreme events were defined by all-time maxima over Africa, firstly by location and then by date. For example, coastal wind storms were identified at Benghazi (8 February 1996), Pt. Elizabeth (9 July 2002), and Beira (14 March 2019). Floods were indicated by ranking daily rainfall and studying associated weather conditions, as follows: (i) the Guinea coast, 1–5 April 2008; (ii) the Congo Basin, 1–20 March 2020; and (iii) the Mozambique coast, 20–24 January 2021. These case studies employ Cloudsat reflectivity, hourly ERA5 field data, and multi-satellite rainfall. Tropical cyclone intensity and tracks near Madagascar were analyzed. To examine the characteristics of arid coasts, springtime (September–November) upwelling off Namibia was studied via ocean reanalysis [34], at a 27S depth section from 8–16E, 1–800 m. Maps of minimum SST and rainfall were analyzed and mean afternoon winds and boundary layer heights were calculated.

Temporal analyses focus on spatial clusters identified via the application of the empirical orthogonal function (EOF) to monthly CRU4 PDSI fields from 1970 to 2020, namely Sahel 7.5–16N, 5–35E; Southern Africa 30–15S, 20–33E; and East Africa 10S–7N, 28–38E. Regional PDSI (P–E) anomaly time series are based on an average of CRU4 and ERA5, to offset declining in situ station measurements with increasing remote sensing observations [35,36]. The PDSI records were subjected to a low-pass 18 month polynomial

filter, to preserve interannual variability and trend. The three regional PDSI time series were then subjected to wavelet spectral analysis to quantify persistent rhythms with periods of 1–11 years.

Long-term trends were evaluated to determine if the slope of the least-squares linear regression rises above the multi-year variability. This is carried out using an 18 month time series, with 34 degrees of freedom (df) and yearly maps in the satellite era, with 42 df. A temporal correlation coefficient  $> |0.30|$  implies 95% confidence and that the trend is significant. For spatial regressions, the long-term slope is analyzed and shaded above statistical threshold.

The spatial structure of intra-seasonal fluctuations was determined by calculating the standard deviation in 10-day multi-satellite rainfall and vegetation fields over the period 1980–2022. Area-averaged daily net OLR time series were evaluated for the mean annual cycle of the upper and lower 2.5 percentiles and running 3-year standard deviations, to quantify intra-seasonal variance in the following three regions: Sahel, Southern Africa, and East Africa. Long-term trends attributable to climate change from 1979 to 2022 were mapped by calculating the linear regression slope in the fields of daily net OLR, dewpoint temperature, and UV components of the 925–850 hPa wind, which were subsequently recombined into vectors.

The Hadley earth system model (esm) coupled ensemble model [37] simulated maximum daily rainfall, while monthly potential evaporation fields were compared with observations, in the context of surface roughness and irrotational airflow convergence, as indicated by a positive 850 hPa velocity potential. Alternatively, CMIP5 projected maximum daily rainfall, as is presented in Appendix A, from the CNRM, IPSL, and MIROC coupled ensemble models, using IPCC methodology [38].

During the initial data exploration stage, some discrepancies were found in ERA5 hindcast products before 1970, in daily satellite rainfall before 1998, and in CRU4 interpolated fields since 2010. Hence, the survey methods are intended to curb the interpretation of artificial outcomes.

### 3. Results

#### 3.1. Geography and Climatology

One-third of Africa is covered by sub-tropical deserts that release dust aerosols in dense concentrations  $>500 \mu\text{g}/\text{m}^3$  (Figure 1a), largely during summer. The dust tends to scatter incoming radiation and reduce the efficiency of moist convection over the Sahel. Farm encroachment around the Congo Basin has denuded swaths of tropical forest, generating smoke plumes, mainly during the spring season. Carbon monoxide concentrations  $>200$  ppb spread across the continent, as detected using satellite radiometers (Figure 1b). The smoke and dust plumes often sweep westward over the Atlantic Ocean. Africa's biomass burning produces  $\sim 14\%$  of the global greenhouse gas emissions ( $\text{CO}_2$  eq  $\sim 1.4 \times 10^{12}$  kg/year), which alters the radiation budget, leading to global warming [39,40]. Numerous rivers flow out of tropical Africa (Figure 1c)—Congo (avg  $42 \sigma \pm 16$ ), Niger ( $8 \pm 3$ ), Zambezi ( $4 \pm 1$ ), Nile ( $3 \pm 5$ ), and Madagascar ( $\times 10^3 \text{ m}^3/\text{s}$ ). Africa may appear to be well endowed with water supplies, but long-term average potential evaporation losses exceed 6 mm/day across the vast semi-arid sub-tropics and 2 mm/day over the Congo basin, coastal margins, and scattered highlands (Figure 1d). The all-Africa long-term mean rainfall of 2 mm/day, against a potential evaporation of 4 mm/day, generates water scarcity that is characterized by a soil moisture of 30% and a run-off of 0.5 mm/day [41]. The thirsty landscape requires scientific knowledge to optimize the management of limited resources.

#### 3.2. Spatial Pattern of Extremes

Daytime land surface temperatures and linear trends, as determined using an IR satellite, are presented in Figure 2a,b. Three zones of  $\sim 60^\circ\text{C}$  temperatures appear—southern Algeria 25N, 0E; Nile Valley 15N, 30E; and southern Namibia 25S, 20E. Daytime land surface temperatures are moderated by moist soils in the Congo Basin and along the coasts of

Guinea, east Madagascar, and South Africa. Warming trends  $+0.05\text{ }^{\circ}\text{C}/\text{year}$  are notable over the highlands of East Africa, Southern Africa, and Madagascar, as well as across the Sahara Desert. However, trends are negligible (insignificant) over wide swaths of the Congo and Guinea monsoons and Okavango savannah. Outcomes suggest that highlands should be managed to retain ground cover.

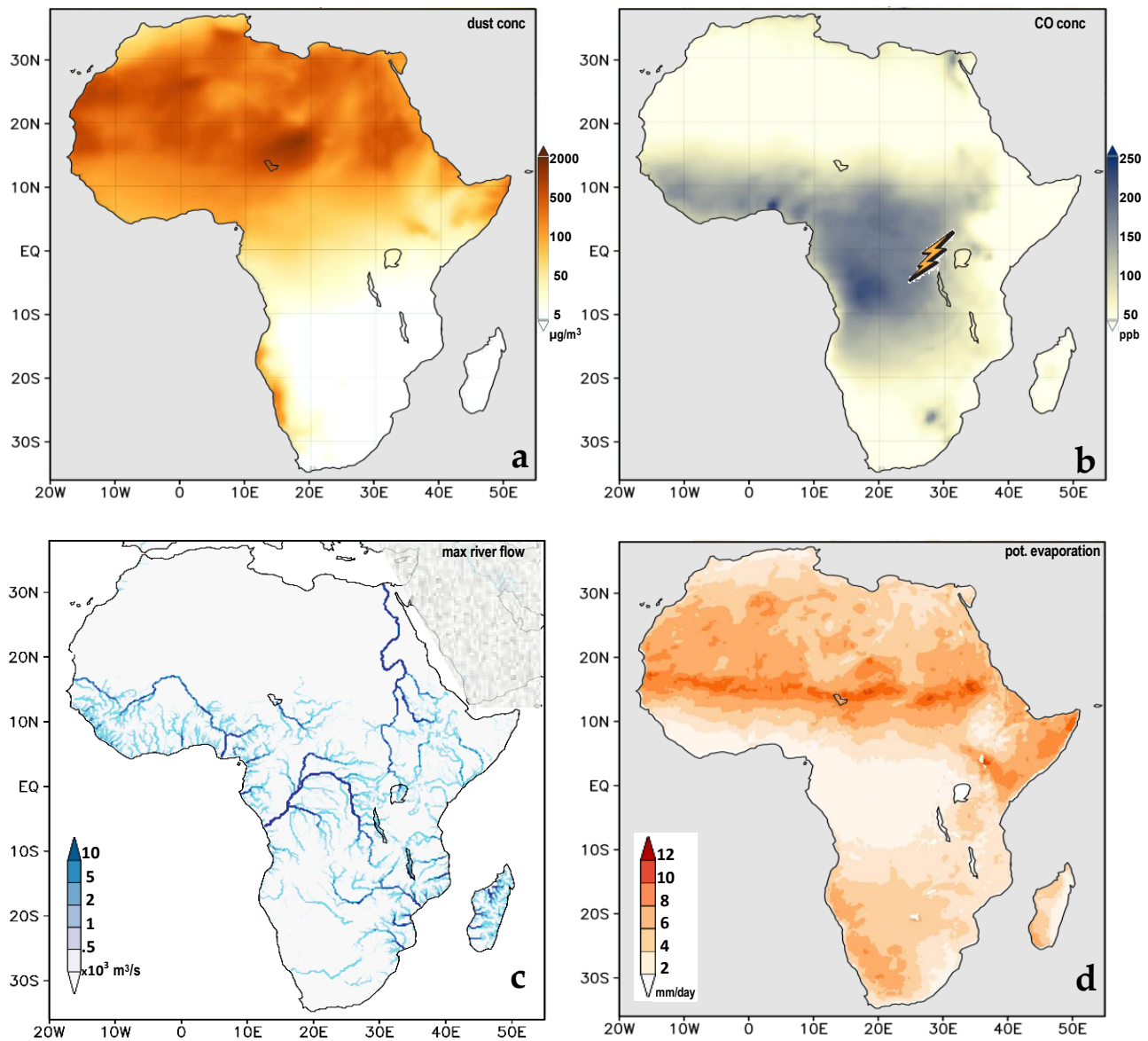


**Figure 1.** Long-term average concentration maps of (a) surface dust ( $\mu\text{g}/\text{m}^3$ ) and (b) carbon monoxide (smoke, ppb), with lightning icon at maximum ( $>100$  flashes  $\text{km}^{-2}/\text{year}$ ). (c) All-time maximum daily river discharge (log-scale  $10^3\text{ m}^3/\text{s}$ ) and (d) long-term mean potential evaporation. Note that results over adjacent continents and oceans are masked, to focus on Africa.

Cold and warm extreme daily air temperatures are mapped in Figure 2c,d. Naturally, the northern and southern mid-latitudes experience cold fronts during winter, which depress mean temperatures to  $<10\text{ }^{\circ}\text{C}$ , particularly in the Atlas and Drakensberg mountains. At elevations above 2000 m, frost is frequent and minimum temperatures near  $-20\text{ }^{\circ}\text{C}$  have been recorded during winter in Morocco and Lesotho. Summer heating in the vast Sahara and smaller Kalahari Deserts contributes to large areas with mean temperatures  $>35\text{ }^{\circ}\text{C}$ ; maximum temperatures near  $50\text{ }^{\circ}\text{C}$  have been measured during summer in Algeria and Namibia.

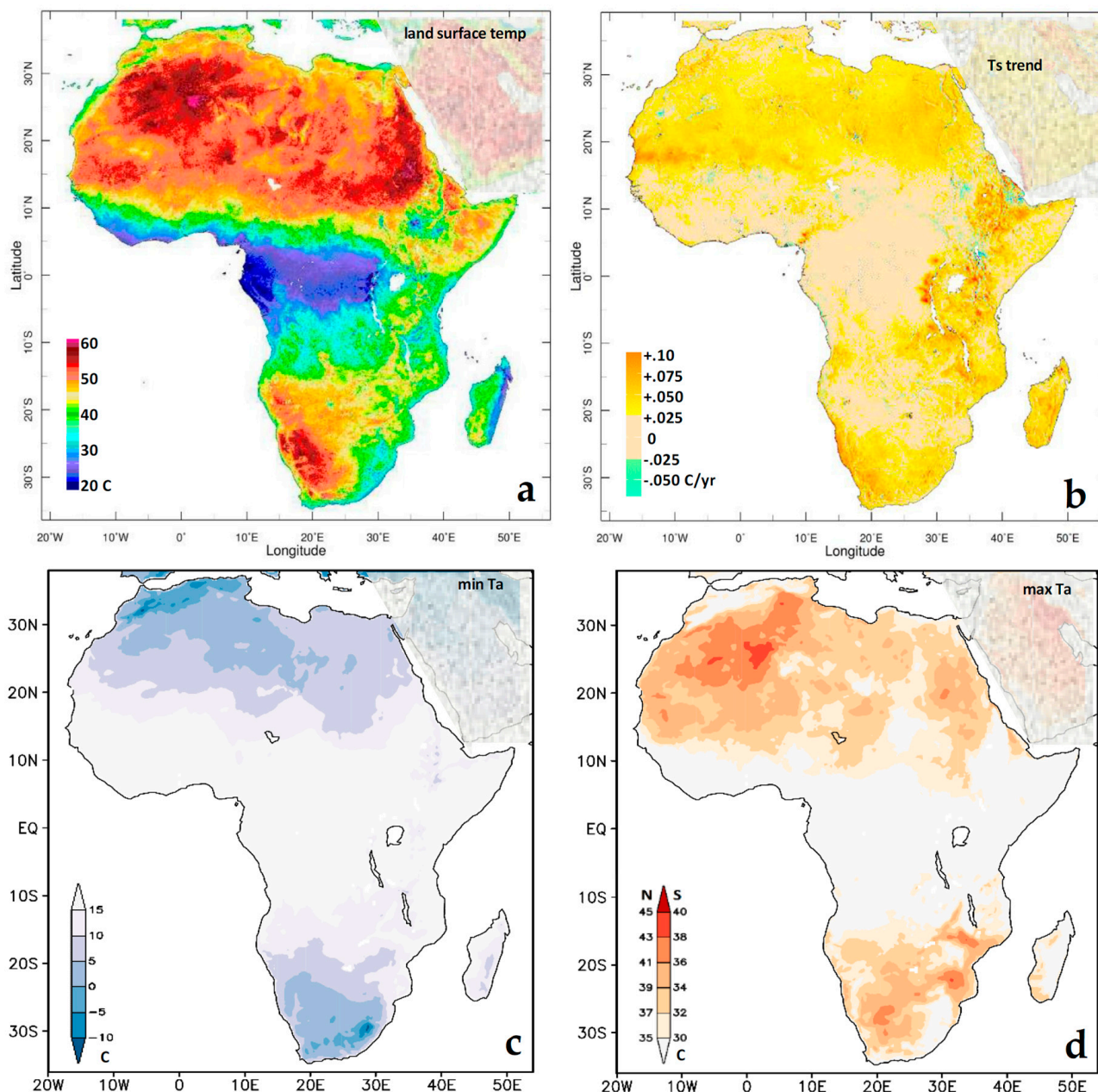


**Figure 2.** (a) Daytime land surface temperature (satellite IR) and (b) linear trend of land surface temperature ( $^{\circ}\text{C}/\text{year}$ ), 1980–2020 (neutral shading  $\pm 0.02\text{ }^{\circ}\text{C}/\text{year}$  is insignificant), (c) maps of lowest daily air temperature  $< 15\text{ }^{\circ}\text{C}$  (blue), and (d) highest daily air temperature  $> 30\text{ }^{\circ}\text{C}$  (south)  $> 35\text{ }^{\circ}\text{C}$  (north); warm spells across the Sahara require a higher threshold.

The wind circulations and extremes are shown in Figure 3a–f. The Indian Ocean monsoon reversal dominates the eastern flank of Africa, in contrast with anticyclonic equatorward winds along the Atlantic-facing coast. The Guinea zone shows an SW monsoon in June–August, while NE winds sweep across the eastern Sahara in December–February. A perennial low-level ‘jet’ of warm, dry air flows into the Turkana Valley (Kenya). Coastal winds are strong along the southeast and northwest coasts. Naturally, the Hadley Cell (Figure 3c,d) oscillates north–south, following the sun; the broad meridional overturning in December–February is replaced by a more complex circulation in June–August that rises slantwise from Sahel to Congo. Maximum wind speeds (Figure 3e) reflect marine storms that sweep along the north and south coasts during winter, as well as along the Mozambique Channel in summer (December–April).

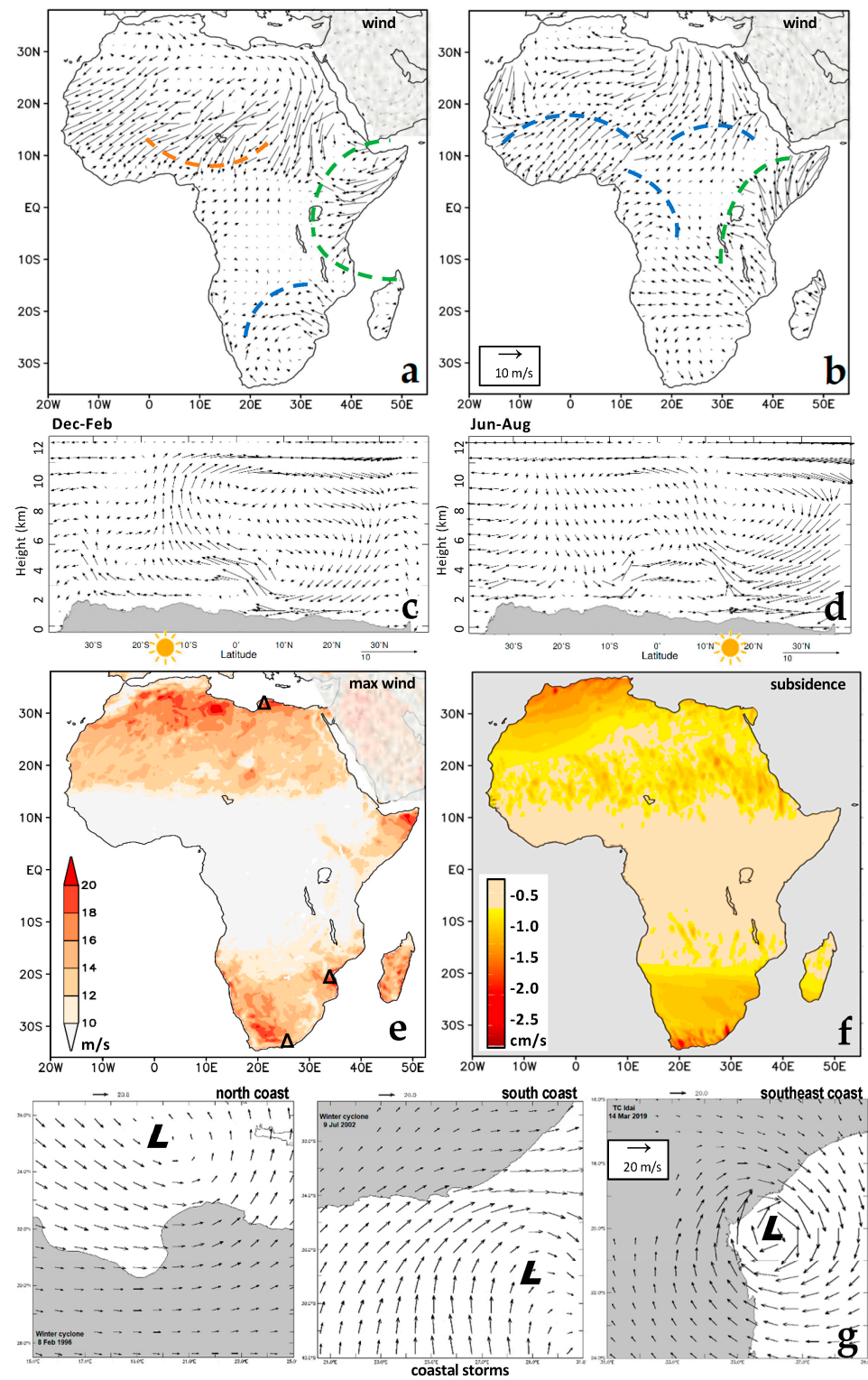


**Figure 3.** Seasonal mean terrestrial 925–850 hPa wind circulation in (a) December–February and (b) June–August, with dashed airflow boundaries and (c,d) height section of corresponding Hadley circulation averaged 20–30E, with seasonal sun icon and topographic profile. (e) Maximum surface wind speed (m/s) with locations of events  $\Delta$  in g below, (f) maximum 500 hPa subsidence (cm/s) with oceans masked, and (g) extreme coastal wind events at (left to right) Benghazi, Libya; Pt Elizabeth, South Africa; and Beira, Mozambique (land shaded), vector scale 20 m/s.

The maximum 500 hPa subsidence (Figure 3f) exhibits broad sweeping features associated with anticyclonic shear from jet streams [42], as well as negative heat fluxes, over sub-tropical upwelling zones in northwest and Southern Africa. Isolated streaks of strong subsidence are located along 15N and 15S, associated with intra-seasonal wave motions. Three wind events are highlighted in Figure 3g—winter storms along the coast at Benghazi 32N, 21E and Pt Elizabeth 34S, 26E, and a tropical cyclone at Beira 20S, 35E. These storms damage coastal infrastructure and rural ecosystems. The winter storms bring big waves and cold temperatures, while the tropical cyclones generate storm surges followed by flash floods that displace communities in Mozambique [43] and the lower Zambezi Valley.

### 3.3. Regional Evaluation of Inter-Annual Climate

The outcome of the EOF analysis applied to CRU4 PDSI fields from 1970 to 2022 is presented in Figure 4a–c. Three clusters emerge from the spatial loading patterns—Sahel 7.5–16N, 5–35E (23% variance); Southern Africa 30–15S, 20–33E (19%); and East Africa 10S–7N, 28–38E (10%). Due to the low amplitude of year-to-year variability, the Congo is the fourth mode (7%). The smoothed PDSI anomaly time series, based on CRU4 and ERA5, reveal that the Sahel experienced wet spells in the 1970s, then drought in the 1980s, followed by multi-year fluctuations. Similarly, Southern Africa had  $P > E$  in the 1970s, then drought in the 1980s and 1990s, followed by neutral conditions. East Africa experienced diminishing wet spells from the 1970s to the 1990s, drought from 2000 to 2005, and wet spells in recent years. Wavelet spectra exhibit oscillations at 3 year intervals from the Indian Ocean Dipole (IOD) and ocean Rossby waves [44,45]. Wavelet spectra also show 5–6 years fluctuations of PDSI for East Africa and a 10–11 years periodicity for the Sahel and Southern Africa. Trends were small compared with large inter-decadal oscillations, which are most intense in Southern Africa, due to ENSO–IOD seasonality.

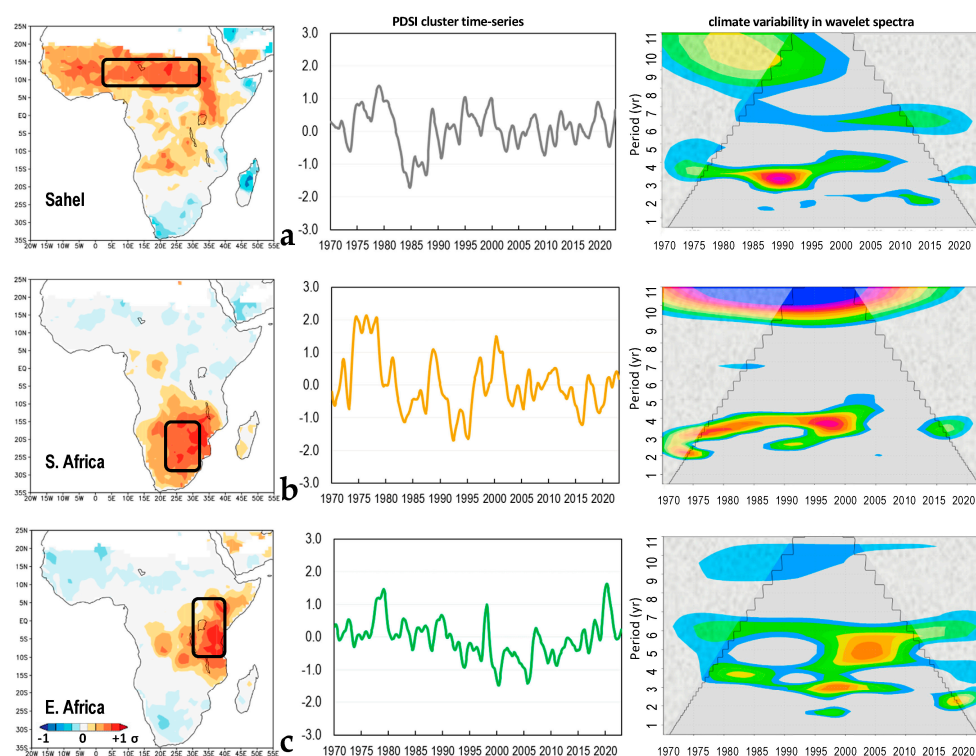


**Figure 4.** (left) EOF clusters that define regions (boxes) based on CRU4 PDSI (P–E anomalies), from the top down (a) Sahel, (b) Southern Africa, and (c) East Africa. (Middle) 18-month polynomial filtered P–E time series per region and (right) inter-annual wavelet spectral energy (rainbow shaded from 90 to 99% confidence within the cone of validity). EOF shading (left) is standardized ( $\sigma$ ).

### 3.4. Intra-Seasonal Variability

The maximum rainfall is mapped via ERA5 and cMorph products in Figure 5a,b, for the period of microwave satellite coverage from 1998 to 2023. These show spots of heavy rain around the Mozambique Channel and the Guinea coast, associated with maximum SST > 30 °C. cMorph indicates more floods (>100 mm/day) in the Congo Basin and Zambezi Valley. Differences may be attributed to data assimilation and model interpolation. The standard deviation of 10-day rainfall is mapped in Figure 5c and shows a high amplitude over Madagascar, the Guinea coast, and the East Africa highlands, while Southern Africa has a lower amplitude. Large intra-seasonal fluctuations of vegetation color (Figure 5d) are evident along swaths from Ethiopia across the Sahel (10N) and from Tanzania across the Zambezi (15S). Agricultural production in these zones is sensitive to changeable weather and would benefit from accurate forecasts, to manage risks.

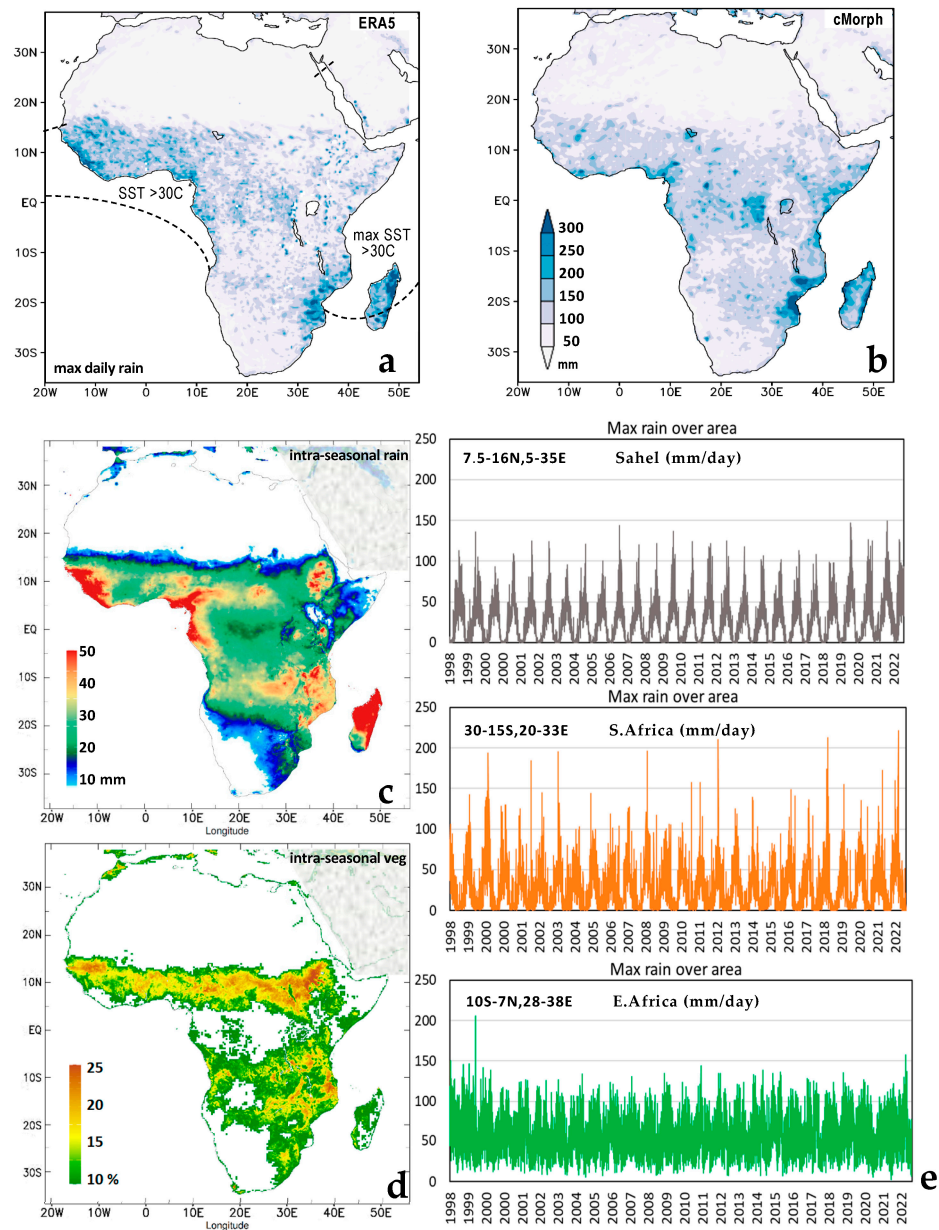


**Figure 5.** Maximum daily rainfall > 50 mm/day: (a) ERA5 with max SST > 30 °C dashed, (b) cMorph multi-satellite 1998–2022, using scale on the right. Intra-seasonal standard deviation of 10-day satellite: (c) rainfall (mm) and (d) vegetation color (%). (e) Time series of maximum rainfall within regions (top to bottom) Sahel, S. Africa, and E. Africa.

The time series of maximum daily rainfall in three regions is presented in Figure 5e. The Sahel and Southern Africa exhibit seasonal floods in late summer, while East Africa’s bi-modal climate has floods scattered throughout the year. Ranking the daily values (Table 2) found many cases of intense rainfall in recent years—Southern Africa in February 2023 (222 mm/day) and March 2019 (213 mm/day); East Africa in June 1999 (206 mm/day) and March 2023 (157 mm/day); and the Sahel in August 2022 (149 mm/day) and August 2020 (147 mm/day).

**Table 2.** Ranked maximum daily rainfall in three regions (1998–2023), date format (yyyy mm dd) and amount (mm), based on an average of three products—ERA5, cMorph, GPM.

	Sahel		S Africa		E Africa
19 August 2022	149	27 February 2023	222	6 June 1999	206
1 August 2020	147	15 March 2019	213	26 March 2023	157
25 July 2007	144	20 January 2013	210	12 January 1998	151
9 August 2020	141	28 January 2009	196	29 January 1999	146
6 August 2020	140	23 January 2004	195	5 October 1998	145
8 August 2010	137	23 February 2000	194	10 January 1998	144
12 August 2022	136	22 February 2000	190	25 November 2011	144
21 June 1999	136	19 July 2002	184	4 November 1999	142
25 July 2021	126	15 February 2019	174	7 May 2015	139
25 April 2023	126	11 April 2022	173	7 April 2000	139

### 3.5. Extreme Cases: Congo Monsoon and Coastal Events

The cases below were identified by ranking extremes within prescribed regions, to reveal the meteorological characteristics of monsoons, storms, and upwellings.

The Congo monsoon is a perennial feature with cloud cover >70% (Figure 6a). A case study in March 2020 shows how equatorial convection builds as sub-tropical upper westerly winds intensify (Figure 6b,c). The Hadley cell responds with meridional overturning and slanted uplift. Diurnal cycles in thermal instability and transpiration generate afternoon rainfall >2 mm/h over the Congo basin (Figure 6d). Cloudsat reflectivity sections (Figure 6e) show deep clouds, >30 dBz, spreading eastward from the warm Gulf of Guinea [46], which caused a tremendous surge of Congo River flow in March–April 2020.

Figure 7a illustrates the tracks of all (75) tropical cyclones passing Madagascar in the period from December to April 1990–2023. Curvature around the Mascarene anticyclone results in westward motion 10–15S, followed by a southward turn. The highlands of Madagascar disrupt TC structure, so they weaken and re-group over the warm Mozambique Channel. The Indian Ocean Dipole (IOD) and Pacific ENSO alter SST and wind shear. TCs bring copious rainfall and big swells, as seen in the January 2021 case study (Figure 7b,c). The NE Indian monsoon is drawn toward the Mozambique Channel during storm intensification. Since 2000, TCs passing Madagascar have become more frequent (~2/year).

Considering the SW monsoon in the Gulf of Guinea, Figure 8a–c analyze an extreme wet spell in April 2008. Meridional sections on 2 and 5 April 2008 show an overturning low-level onshore/upper-level offshore circulation that draws convective clouds from the warm Gulf of Guinea toward coastal cities. The SW monsoon interacts with mid-level easterly waves, as seen in the Hovmöller plot of satellite rainfall. Moisture fluxes are enhanced by cross-equatorial winds that undergo rapid air mass modification over the tropical east Atlantic.

Extreme cases

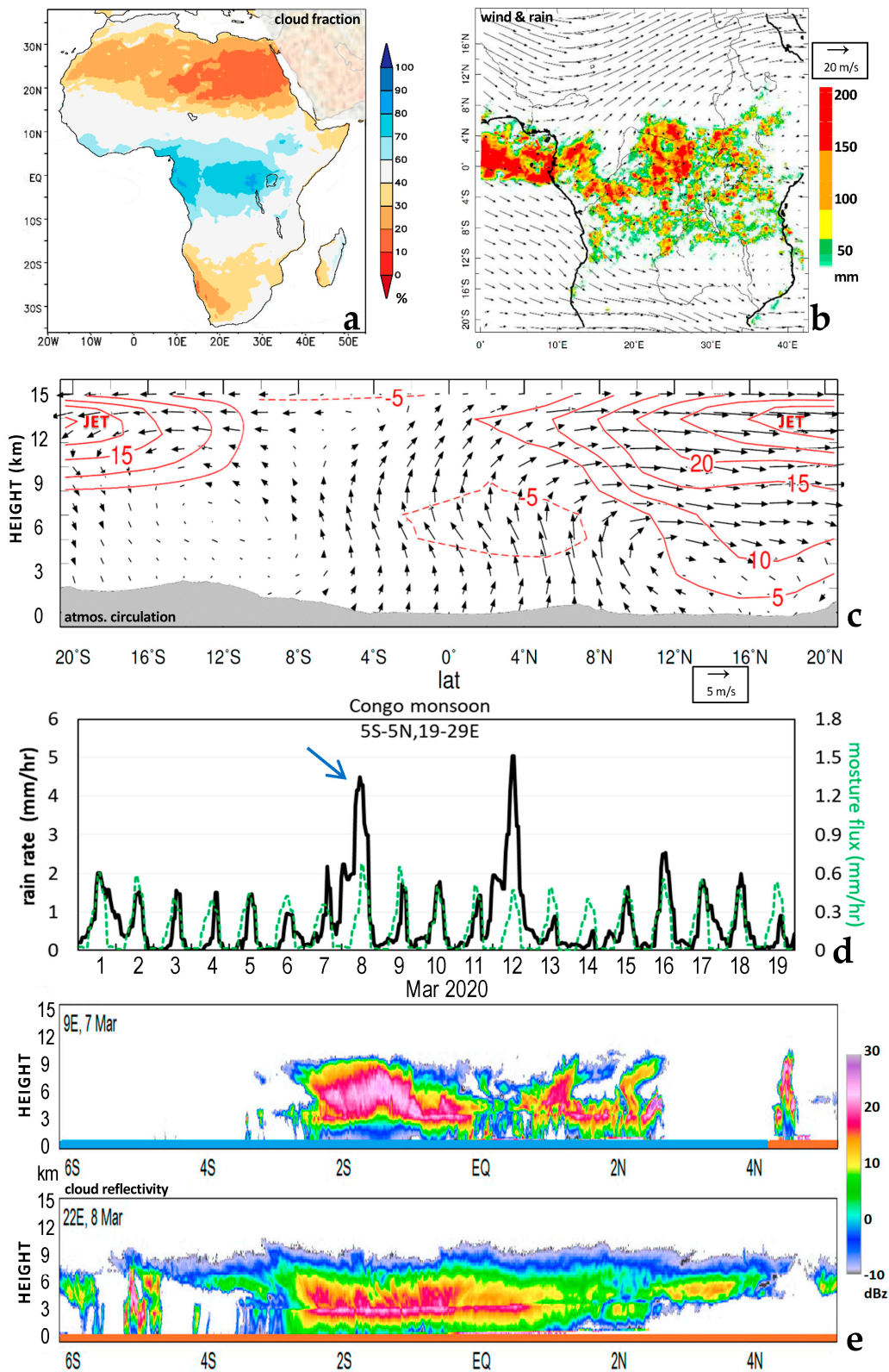


**Figure 6.** Congo monsoon. (a) Long-term mean satellite terrestrial cloud fraction, (b) 250 hPa wind vectors (scale 20 m/s) and GPM satellite rainfall for extreme wet spell, 7–8 March 2020, (c) height section of meridional Hadley circulation (vector) and zonal wind (contour m/s, upper ‘jet’) averaged 9–22E on 7–8 March 2020, (d) time series of ERA5 hourly rain rate and surface moisture flux averaged over the Congo Basin, and (e) Cloudsat reflectivity sections along 9E on 7 March (upper) and 22E on 8 March 2020.

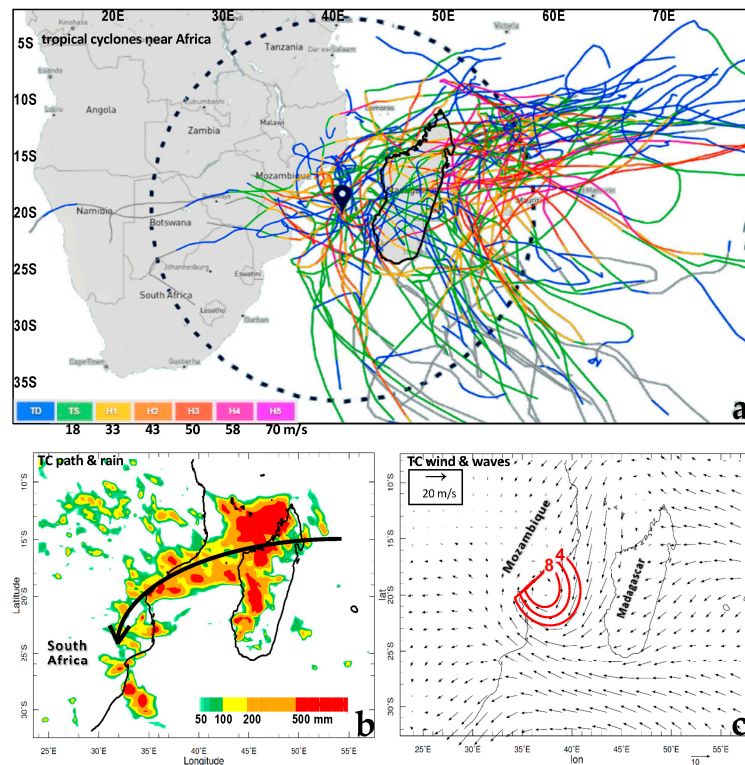


**Figure 7.** (a) Tropical cyclone tracks passing Madagascar (dashed target) in December–April 1990–2022 (colors refer to intensity (max. speed, m/s)), the coast of Madagascar is outlined. (b) Cumulative rainfall on 20–24 January 2021 during intense TC Eloise (track arrow) and (c) 925–850 hPa wind (vector) and wave height (m) red contours on 22 January 2021.

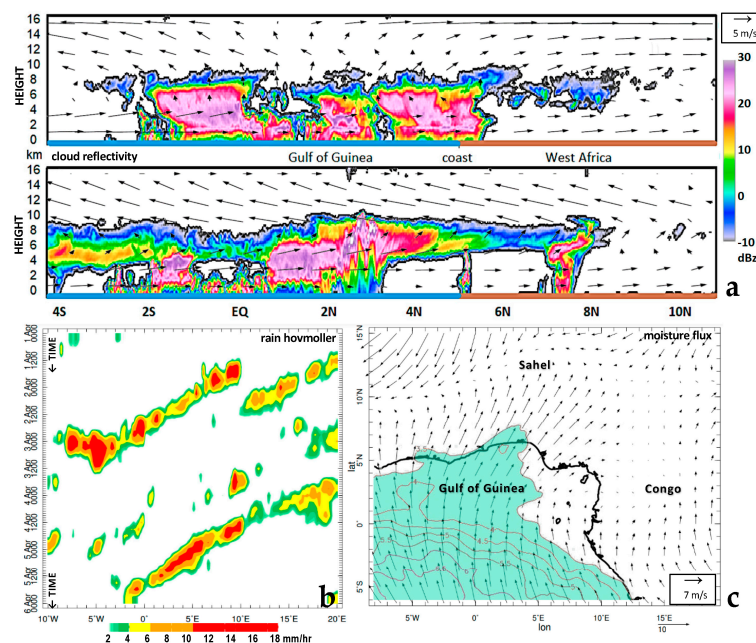


**Figure 8.** (a) Cloudsat reflectivity sections along 5E during a Guinea Coast wet spell on 2 April (upper) and 5 April 2008, with meridional circulation superimposed (largest vector 5 m/s). (b) Satellite rainfall Hovmöller plot averaged 5–7N, indicating easterly waves, and (c) 1–5 April 2008 925–850 hPa winds and moisture flux > 3.5 mm/day green shaded, illustrating SW monsoon surge over the Gulf of Guinea.

Africa has three wind-driven coastal upwelling zones—(i) Morocco to Senegal, (ii) Somalia (in June–August), and (iii) western South Africa to Namibia. The south-east Atlantic’s shallow anticyclonic circulation is vigorous during springtime. Southern Namibia (27S) is a focal point for upwelling (Figure 9a–c). Equatorward winds of 9 m/s from 12–15E, 0–500 m height, drive seawater away from the coast (offshore transport); therefore, cold seawater lifts over the shelf, producing a narrow coastal zone of SST < 11C and rainfall < 0.1 mm/day (Figure 9d). Mean afternoon winds (Figure 9e) respond to land–sea temperature differences with a sea-breeze that pulls away from the longshore airflow, creating divergence and a shallow atmospheric boundary layer. Drought across Southern Africa is linked to westerly winds spreading the dry Benguela airmass [47].

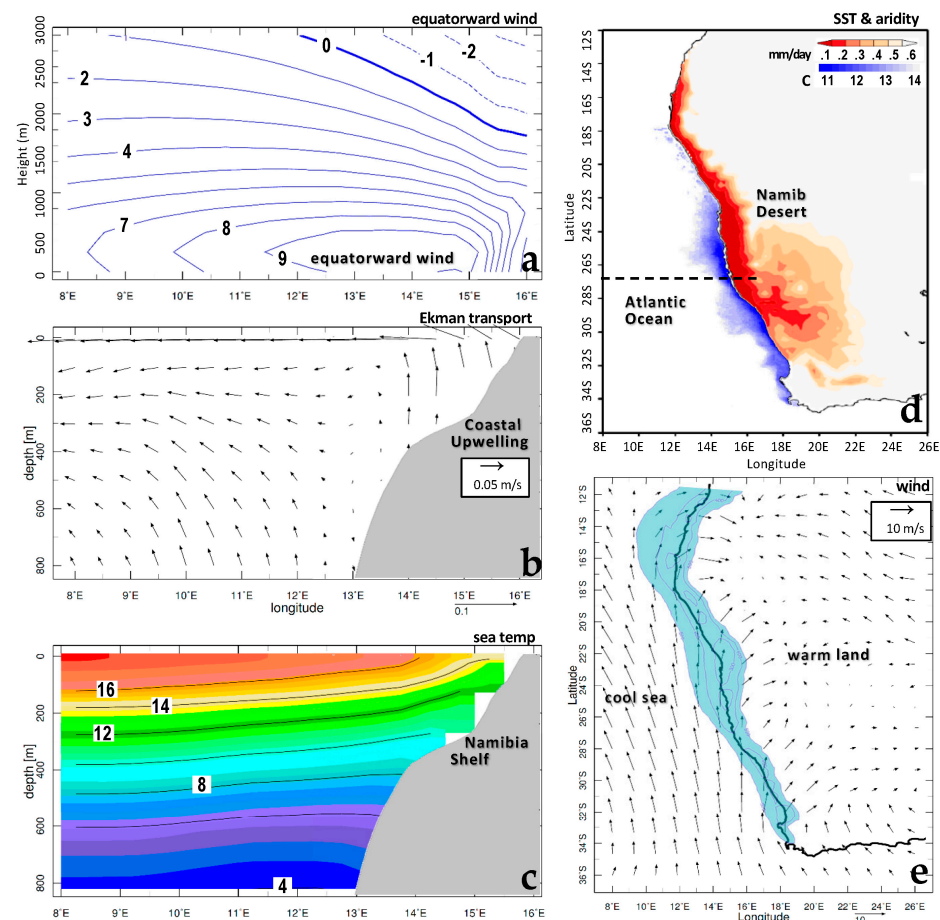


**Figure 9.** (left) Southeast Atlantic marine climate on section 27S, off the coast of Namibia, during extreme upwelling in austral spring, September–November 2011: (a) meridional V wind, (b) ocean zonal circulation, (c) sea temperature (°C). (right) Maps of (d) minimum monthly rainfall and minimum SST (red and blue shaded) in 1990–2022, dashed line (27S) refers to slice at left and (e) September–November surface wind vectors (averaged 12:00–18:00 LST) that diverge in a shallow boundary layer (blue shaded < 500 m) on the Atlantic coast.

### 3.6. The P–E Balance (Net OLR)

Having covered the meteorological features of extremes, here the surface water balance is studied via daily satellite net OLR. The mean pattern in Figure 10a shows areas of net OLR > 275 W/m<sup>2</sup> (E > P) over the vast Sahara and smaller Kalahari Deserts, as well as along the northeast coast (Somalia) and southwestern Madagascar. Areas of net OLR < 255 W/m<sup>2</sup> (P > E) appear over the highlands of East Africa, the Congo Basin, and Guinea coast. Small patches of low values emerge over mid-latitude highlands, due to winter temperatures. Linear trends for annually averaged net OLR from 1979 to 2022 (Figure 10b) are positive (drying) across the southeast and northwest sub-tropics and Madagascar, while they are

negative (moistening) across the western Congo and Guinea coast. The regional mean annual cycles (Figure 10c) of the upper 2.5 percentiles reflect dry spring seasons (Sahel: March, Southern Africa: September), while the lower 2.5 percentiles occur in summer (Sahel: July, Southern Africa: January). East Africa’s bi-modal climate exhibits the lower 2.5 percentiles for net OLR in March and November (rainy seasons). Running 3 years standard deviations (Figure 10d) show increasing daily variance over the Sahel, higher values 1997/2007 for Southern Africa, and low variance in recent decades in most regions. Evidence on rising vulnerability to mesoscale flood and drought [48] raises questions on whether coupled model simulations can detect those signals.

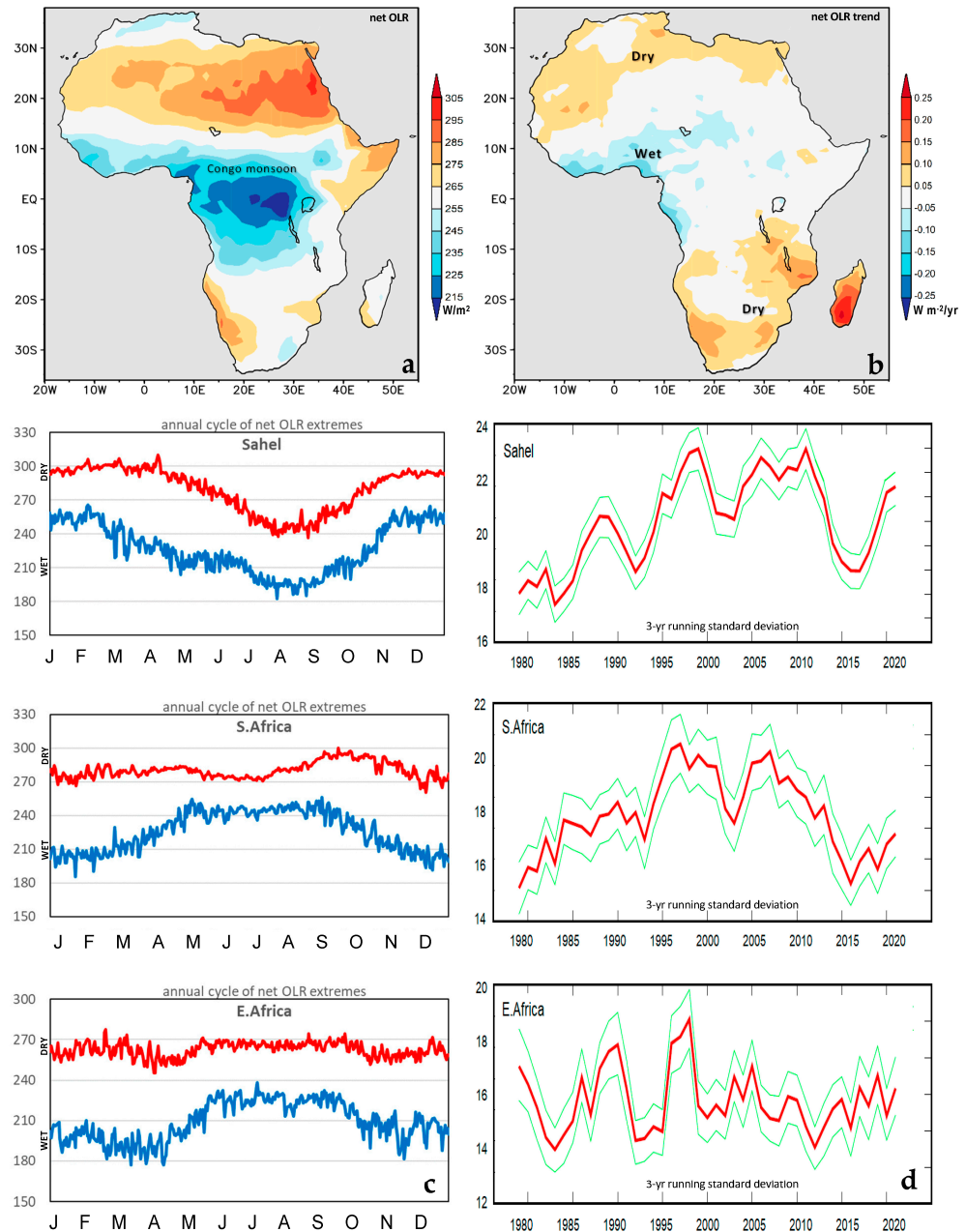


**Figure 10.** (a) Average satellite net OLR ( $W/m^2$ ) and (b) its linear trend ( $W m^{-2}/year$ ) (1979–2022), high values = warm and dry, oceans masked; note that neutral shading is below 90% confidence. (c) Mean annual cycle of upper and lower 2.5 percentiles of daily net OLR and (d) the 3 years running standard deviation of daily net OLR ( $W/m^2$ ), in three regions (top-down)—Sahel, Southern Africa, and Eastern Africa.

### 3.7. Simulations, Trends, and Uncertainties

Figure 11a,b presents a coupled ensemble Hadley model that simulated maximum daily rainfall and mean potential evaporation (1990–2022), for comparison with earlier results. Flood events are lacking across the Congo and Guinea zone, but tropical storms along the Mozambique Channel are consistent with observations. Wet spells appear over the Sahel (13N) and Zambezi (18S) (see Figure A2 for alternative simulations). Potential evaporation spreads from the Sahara and Kalahari Deserts, as expected. Low evaporation is simulated for the Congo and the southern and East Africa highlands, according to the Hadley model. Increasing desiccation is projected for the northern Sahel and eastern Rift Valley; drought risks are growing there.

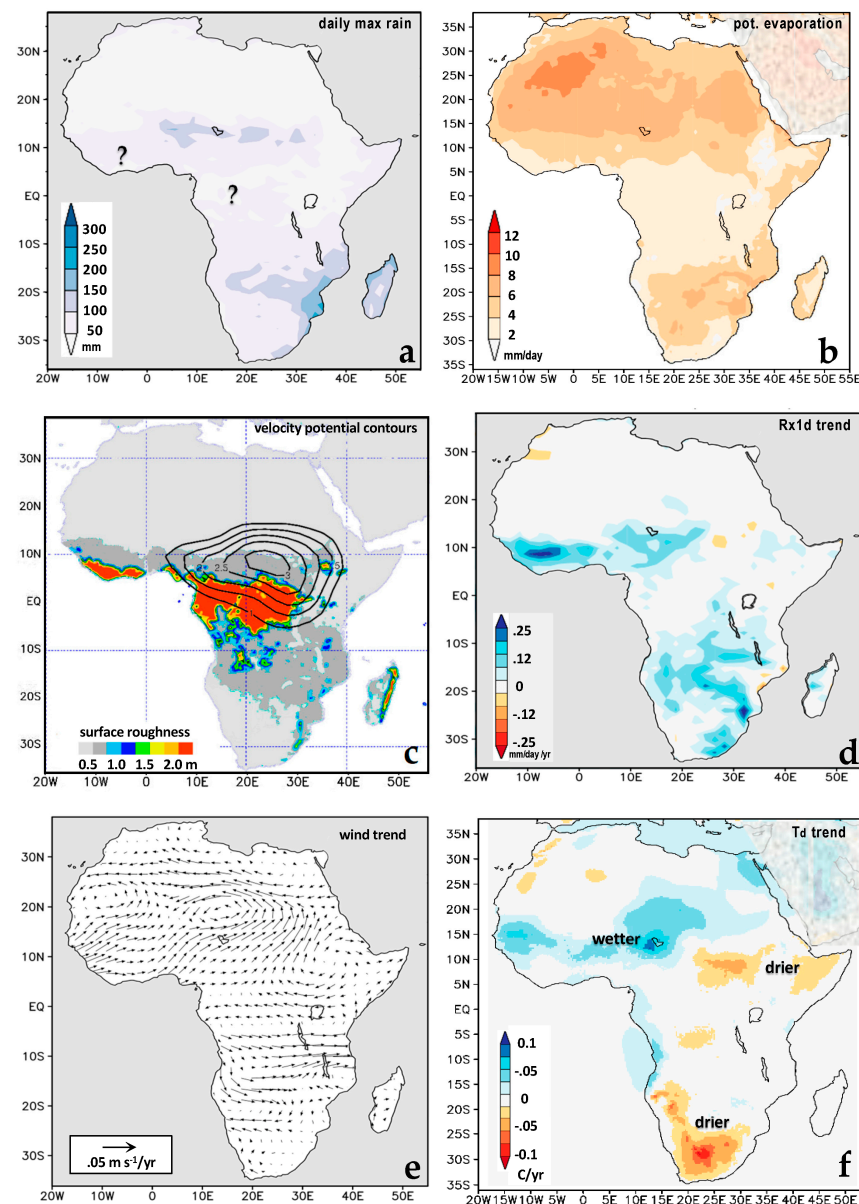


**Figure 11.** Hadley model-simulated: (a) maximum daily rainfall (as in Figure 5a,b) with oceans masked and (b) mean potential evaporation (as in Figure 1d), from 1990 to 2022. (c) Model surface roughness (shaded) and 850 hPa velocity potential contours ( $\times 10^6 \text{ m}^2 \text{ s}^{-1}$  in March 2020, a wet spell), which quantify Congo monsoon convergence. (d) Hadley-simulated trend of annual maximum daily rainfall (mm day<sup>-1</sup>/year) from 1980 to 2050, with CO<sub>2</sub> doubling. (e,f) Maps of linear trend in 925–850 hPa wind (vector, m s<sup>-1</sup>/year) and ERA5 dewpoint temperature (°C/year) from 1979 to 2022. For alternative model-simulated maximum daily rainfall, see Figure A2.

Surface roughness (Figure 11c) is a static descriptor of terrain and canopy undulations embedded in weather and climate models. Moisture fluxes may be inhibited by numerically parameterized friction over tropical rain forests. During equatorial wet spells, such as March 2020 (see Figure 6), that amplify Congo River flow, 850 hPa velocity potential contours  $> 10^6 \text{ m}^2 \text{ s}^{-1}$  overlie the zone of surface roughness  $> 1 \text{ m}$ . Convergent airflow slows and lifts, causing deep convection; this is a process that could be under-represented in coupled ensemble models.

Discrepancies in station data assimilation were mentioned earlier. Data in Appendix A show that in situ measurements have declined in all regions since the 1990s (Figure A1) and large areas have limited coverage, a common feature in African datasets [9,49]. Artificial outcomes are generated in data-sparse regions, hence PDSI time series were averaged using CRU4 and ERA5 P–E. Declining station networks inhibit the monitoring and forecasting of extreme weather. It is recommended that national meteorological services maintain first order stations in capital cities and just a handful of second order real-time reporting stations elsewhere; ‘less is more’.

Many outcomes suggest links between extreme weather and climate change—dense smoke plumes, rising surface temperatures, and potential evaporation. Long-term trends in daily precipitation, 925–850 hPa wind, and dewpoint temperature from 1980 to 2022 (Figure 11d–f) indicate intensifying mesoscale storms in the Sahel, within an expanding SW monsoon. In contrast, divergent airflows have led to drying trends across the East African Rift Valley and southern Kalahari plateau. Eastward wind trends along 10S (Figure 11e) suggest a growing influence for the tropical Atlantic.

Some results were incoherent, for example the downward trend in Sahel PDSI (Figure 4a) that is indicative of faster evaporation and contrasts with the pattern of maximum daily rainfall (Figure 5a,b, Figures 11a and A2), which is associated with differences in satellite technology and model resolution. These generate uncertainty in our wide-ranging survey and hinder the ability to discern trends that could be translated into strategic planning around climate risks.

#### 4. Concluding Discussion

This study has surveyed African weather and climate extremes and compiled an atlas focusing on the water balance (net OLR and PDSI) across timescales since 1970. Modern high-resolution reanalysis was employed to reveal the patterns and trends embedded within a variable climate. With outcomes underpinned by remote sensing, declining station reports (see Figure A1) [9] have less influence. Satellite air chemistry reflected biomass burning contributions to greenhouse gas emissions amidst frequent lightning. Maps of daily maxima revealed coastal storm impacts around the Mozambique Channel and Gulf of Guinea (for rain), and along the north and south coasts during winter (for wind). Hot weather naturally occurred over the vast Sahara and smaller Kalahari Deserts, as well as the lowland river valleys in the sub-tropics. Similarly, potential evaporation was high across arid zones of southwestern and East Africa and across the Sahel. PDSI and net OLR yielded information on the water balance, which guided regional evaluations. The deepest convection overlies the eastern Congo Basin (215 W/m<sup>2</sup>, 1S, 27E). Net OLR trends were for drying over sub-tropical zones ~30N and ~25S and moistening over the Guinea coast. This survey confirmed the opposing effects of extreme weather and climate change, whereby both daily rainfall and monthly potential evaporation exhibit upward trends from overheated convective turbulence. Land use management that preserves the natural ground cover as a shield from solar insolation would be useful, especially in the semi-arid highlands.

Temporal analysis of area-averaged PDSI, based on [48], averaged with ERA5 P–E, revealed high-amplitude multi-year climate oscillations. PDSI trends were weak and potentially impacted by declining station reports and the inhomogeneity of reanalysis [49]. Yet, an inference can be drawn that extreme events are sufficiently localized, so resource deficits in one region can be covered by surpluses elsewhere. Ranking extreme flood events, many emerged in the recent decade (see Table 2) and point to growing socio-economic vulnerability. The

meteorology of extreme wet and dry spells was explored through case studies. Some drew attention to wind–wave storm surges that lead to coastal erosion under rising sea levels. Other cases showed interactions between coastal monsoons and tropical atmospheric waves, as well as between anticyclonic winds, upwellings, and atmospheric subsidence.

Observations and simulations support the finding that mesoscale convective rainfall and potential evaporation have intensified in recent decades. This survey has identified regions of higher flood risk in the Guinea Coast and Sahel, as well as higher drought risk in Southern Africa and Madagascar. African communities have become resilient in the face of extreme weather and have shown that adaptation can improve the quality of life. Greater mitigating efforts are required so that macro-economic progress does not set in motion harmful secondary consequences (Congo deforestation).

**Funding:** The research received no direct funding.

**Data Availability Statement:** A data spreadsheet is available on request.

**Acknowledgments:** Websites used for data extraction and analysis include Climate Explorer KNMI, IRI Climate Library, Univ Hawaii APDRC, NASA–Giovanni, Coast–NOAA, and Colorado State–Cloudsat. Support from the South Africa Dept of Higher Education is appreciated.

**Conflicts of Interest:** The author declares no conflict of interest.

### Appendix A

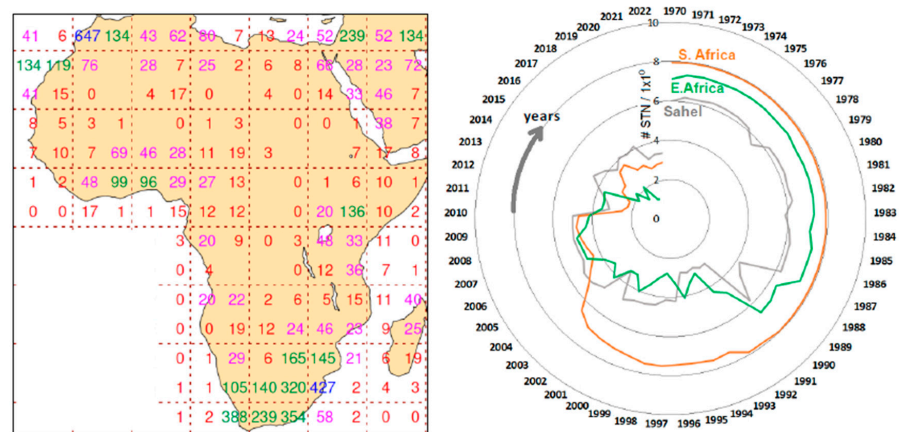


**Figure A1.** (left) Recent map of ECMWF reporting frequency for operational weather stations (values represent #/day/5x5°, 0 = 0.1–0.9, blank = none). (right) Clockwise plot of historical station density in three regions (values represent #/month/1x1°, declining since 1990).

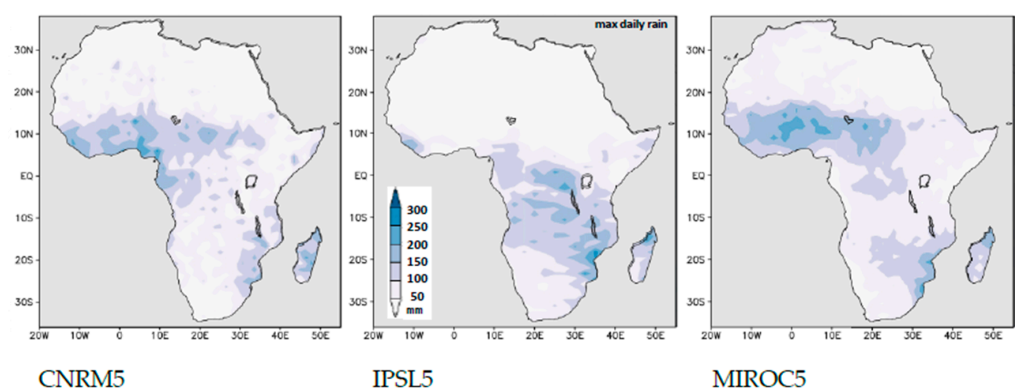


**Figure A2.** Alternative results from coupled ensemble models, for maximum daily rainfall 1990–2022, for comparison with observations and simulation in Figure 5a,b and Figure 11a, all use same scale.

## References

1. Diedhiou, A. Trends in hydrological and climate extremes in Africa. *Atmosphere* **2019**.
2. World Bank Report on Africa's Economic Prospects. 2023. Available online: <https://www.worldbank.org/en/region/afr/overview> (accessed on 30 April 2024).
3. FAO Statistical Database on Production and Macro-Economic Indicators for Africa. 2023. Available online: <https://www.fao.org/faostat> (accessed on 30 April 2024).
4. Water Scarcity in Africa: Causes, Effects and Solutions. 2022. Available online: <https://earth.org/water-scarcity-in-africa> (accessed on 30 April 2024).
5. Marra, F.; Levizzani, V.; Cattani, E. Changes in extreme daily precipitation over Africa: Insights from a non-asymptotic statistical approach. *J. Hydrol.* **2022**, *16*, 100130. [[CrossRef](#)]
6. Taylor, R.G.; Todd, M.C.; Kongola, L.; Maurice, L.; Nahozya, E.; Sanga, H.; MacDonald, A.M. Evidence of the dependence of groundwater resources on extreme rainfall in East Africa. *Nat. Clim. Chang.* **2013**, *3*, 374–378. [[CrossRef](#)]
7. IPCC. The Physical Science Basis. In *WG1 6th Intergov Panel Climate Change*; Masson-Delmotte, V., Zhai, P., Pirani, A., Connors, S.L., Péan, C., Berger, S., Caud, N., Chen, Y., Goldfarb, L., Gomis, M.I., et al., Eds.; Cambridge University Press: Cambridge, UK, 2021; 280p.
8. Washington, R.; Harrison, M.; Conway, D.; Black, E.; Challinor, A.; Grimes, D.; Jones, R.; Morse, A.; Kay, G.; Todd, M. African climate change: Taking the shorter route. *Bull. Am. Meteorol. Soc.* **2006**, *87*, 1355–1366. [[CrossRef](#)]
9. Harrison, L.; Funk, C.; Peterson, P. Identifying changing precipitation extremes in sub-Saharan Africa with gauge and satellite products. *Environ. Res. Lett.* **2019**, *14*, 085007. [[CrossRef](#)]
10. Taylor, C.M.; Belušić, D.; Guichard, F.; Parker, D.J.; Vischel, T.; Bock, O.; Harris, P.P.; Janicot, S.; Klein, C.; Panthou, G. Frequency of extreme Sahelian storms tripled since 1982 in satellite observations. *Nature* **2017**, *544*, 475–478. [[CrossRef](#)] [[PubMed](#)]
11. Vischel, T.; Panthou, G.; Peyrillé, P.; Roehrig, R.; Quantin, G.; Lebel, T.; Wilcox, C.; Beucher, F.; Budiarti, M. Precipitation extremes in the West African Sahel: Recent evolution and physical mechanisms. In *Tropical Extremes, Natural Variability and Trends*; Venugopal, V., Sukhatme, J., Murtugudde, R., Roca, R., Eds.; Elsevier: Amsterdam, The Netherlands, 2019; ISBN 978-0-12-809248-4.
12. Tierney, J.E.; Ummenhofer, C.C.; deMenocal, P.B. Past and future rainfall in the Horn of Africa. *Sci. Adv.* **2015**, *1*, e1500682. [[CrossRef](#)] [[PubMed](#)]
13. Williams, A.P.; Funk, C. A westward extension of the warm pool leads to a westward extension of the Walker circulation, drying eastern Africa. *Clim. Dyn.* **2011**, *37*, 2417–2435. [[CrossRef](#)]
14. Lyon, B. Seasonal drought in the Greater Horn of Africa and its recent increase during the March–May long rains. *J. Clim.* **2014**, *27*, 7953–7975. [[CrossRef](#)]
15. Aguilar, E.; Aziz Barry, A.; Brunet, M.; Ekang, L.; Fernandes, A.; Massoukina, M.; Mbah, J.; Mhanda, A.; Do Nascimento, D.J.; Peterson, T.C.; et al. Changes in temperature and precipitation extremes in western central Africa, Guinea Conakry, and Zimbabwe, 1955–2006. *J. Geophys. Res.* **2009**, *114*, D02115. [[CrossRef](#)]
16. MacKellar, N.; New, M.; Jack, C. Observed and modelled trends in rainfall and temperature for South Africa: 1960–2010. *S. Afr. J. Sci.* **2014**, *110*, 1–13. [[CrossRef](#)]
17. Kruger, A.C.; Nxumalo, M.P. Historical rainfall trends in South Africa: 1921–2015. *Water SA* **2017**, *43*, 285–297. [[CrossRef](#)]
18. Jiang, Y.; Zhou, L.; Tucker, C.J.; Raghavendra, A.; Hua, W.; Liu, Y.Y.; Joiner, J. Widespread increase of boreal summer dry season length over the Congo rainforest. *Nat. Clim. Chang.* **2019**, *9*, 617–622. [[CrossRef](#)]
19. Yeshanew, A.; Jury, M.R. North African climate variability, part 1: Tropical thermocline–coupling. *Theor. Appl. Climatol.* **2007**, *89*, 25–36. [[CrossRef](#)]
20. Funk, C.; Hoell, A.; Shukla, S.; Blade, I.; Liebmann, B.; Roberts, J.B.; Robertson, F.R.; Husak, G. Predicting East African droughts using Pacific and Indian Ocean sea surface temperature indices. *Hydrol. Earth Syst. Sci.* **2014**, *18*, 4965–4978. [[CrossRef](#)]
21. Nicholson, S.E. Climate and climatic variability of rainfall over eastern Africa. *Rev. Geophys.* **2017**, *55*, 590–635. [[CrossRef](#)]
22. Palmer, P.I.; Wainwright, C.M.; Dong, B.; Maidment, R.I.; Wheeler, K.G.; Gedney, N.; Hickman, J.E.; Madani, N.; Folwell, S.S.; Abdo, G.; et al. Drivers and impacts of Eastern African rainfall variability. *Nat. Rev. Earth Environ.* **2023**, *4*, 254–270. [[CrossRef](#)]
23. Hastenrath, S. Zonal circulations over the equatorial Indian Ocean. *J. Clim.* **2000**, *13*, 2746–2756. [[CrossRef](#)]
24. Xie, S.-P. Global warming: Thermodynamic effects. In *Coupled Atmosphere–Ocean Dynamics*; Elsevier: Amsterdam, The Netherlands, 2023; Chapter 13; pp. 339–366.
25. Hersbach, H.; Bell, B.; Berrisford, P.; Hirahara, S.; Horányi, A.; Muñoz-Sabater, J.; Nicolas, J.; Peubey, C.; Radu, R.; Schepers, D.; et al. The ERA5 global reanalysis. *Q. J. R. Meteorol. Soc.* **2020**, *146*, 1999–2049. [[CrossRef](#)]
26. Lee, H.T.; Gruber, A.; Ellingson, R.G.; Laszlo, I. Development of the HIRS outgoing longwave radiation climate dataset. *J. Atmos. Ocean. Technol.* **2007**, *24*, 2029–2047. [[CrossRef](#)]
27. McMahon, T.A.; Peel, M.C.; Lowe, L.; Srikanthan, R.; McVicar, T.R. Estimating actual, potential, reference crop and pan evaporation using standard meteorological data: A pragmatic synthesis. *Hydrol. Earth Syst. Sci.* **2013**, *17*, 1331–1363. [[CrossRef](#)]
28. Harris, I.; Osborn, T.J.; Jones, P.; Lister, D. Version 4 of the CRU TS monthly high-resolution gridded multivariate climate dataset. *Sci. Data* **2020**, *7*, 109. [[CrossRef](#)] [[PubMed](#)]
29. Pinzon, J.E.; Tucker, C.J. A non-stationary 1981–2012 AVHRR NDVI3g time series. *Remote Sens.* **2014**, *6*, 6929–6960. [[CrossRef](#)]
30. Hulley, G.; Freepartner, R.; Malakar, N.; Sarkar, S. *MODIS Land Surface Temperature and Emissivity Product (User Guide 6)*; NASA-GSFC-JPL: Pasadena, CA, USA, 2016.

31. Hou, A.Y.; Kakar, R.K.; Neeck, S.; Azarbarzin, A.A.; Kummerow, C.D.; Kojima, M.; Oki, R.; Nakamura, K.; Iguchi, T. The Global Precipitation Measurement mission. *Bull. Am. Meteorol. Soc.* **2014**, *95*, 701–722. [[CrossRef](#)]
32. Harrigan, S.; Zsoter, E.; Alfieri, L.; Prudhomme, C.; Salamon, P.; Wetterhall, F.; Barnard, C.; Cloke, H.; Pappenberger, F. GloFAS-ERA5 operational global river discharge reanalysis 1979–present. *Earth Syst. Sci. Data* **2020**, *12*, 2043–2060. [[CrossRef](#)]
33. Gelaro, R.; McCarty, W.; Suárez, M.J.; Todling, R.; Molod, A.; Takacs, L.; Randles, C.A.; Darmenov, A.; Bosilovich, M.G.; Reichle, R.; et al. The modern-era retrospective analysis for research and applications, v2 (MERRA2). *J. Clim.* **2017**, *30*, 5419–5454. [[CrossRef](#)] [[PubMed](#)]
34. Carton, J.A.; Chepurin, G.A.; Chen, L. SODA-3 a new ocean climate reanalysis. *J. Clim.* **2018**, *31*, 6967–6983. [[CrossRef](#)]
35. Wells, N.; Goddard, S.; Hayes, M.J. A self-calibrating Palmer Drought Severity Index. *J. Clim.* **2004**, *17*, 2335–2351. [[CrossRef](#)]
36. Bengtsson, L.; Hagemann, S.; Hodges, K.I. Can climate trends be calculated from reanalysis data? *J. Geophys. Res. Atmos.* **2004**, *109*. [[CrossRef](#)]
37. Williams, K.D.; Copestake, D.; Blockley, E.W.; Bodas-Salcedo, A.; Calvert, D.; Comer, R.; Davis, P.; Graham, T.; Hewitt, H.T.; Hill, R.; et al. The Met Office global coupled model 3.0 configurations. *J. Adv. Model. Earth Syst.* **2017**, *10*, 357–380. [[CrossRef](#)]
38. Stouffer, R.J.; Eyring, V.; Meehl, G.A.; Bony, S.; Senior, C.; Stevens, B.; Taylor, K.E. CMIP5 scientific gaps and recommendations for CMIP6. *Bull. Am. Meteorol. Soc.* **2017**, *98*, 95–105. [[CrossRef](#)]
39. Jury, M.R.; Whitehall, K. Warming of an elevated layer over Africa. *Clim. Chang.* **2010**, *99*, 229–245. [[CrossRef](#)]
40. Ramo, R.; Roteta, E.; Bistinas, I.; van Der Werf, G.I. African burned area and fire carbon emissions are strongly impacted by small fires undetected by coarse resolution satellite data. *Proc. Natl. Acad. Sci. USA* **2021**, *118*, e2011160118. [[CrossRef](#)] [[PubMed](#)]
41. Karamage, F.; Liu, Y.; Fan, X.; Francis Justine, M.; Wu, G.; Liu, Y.; Zhou, H.; Wang, R. Spatial relationship between precipitation and runoff in Africa. *Hydrol. Earth Syst. Sci.* **2018**, *2018*, 1–27. [[CrossRef](#)]
42. Chikoore, H.; Jury, M.R. South African drought deconstructed. *Weather. Clim. Extrem.* **2021**, *33*, 100334. [[CrossRef](#)]
43. Jury, M.R.; Matyas, C. Tropical cyclones in the northern Mozambique Channel: Composite intra-seasonal forcing and 2019 event. *Meteorol. Atmos. Phys.* **2022**, *134*, 70. [[CrossRef](#)]
44. White, W.B. Coupled Rossby waves in the Indian Ocean on interannual time scales. *J. Phys. Oceanogr.* **2000**, *30*, 2972–2989. [[CrossRef](#)]
45. Yamagata, T.; Behera, S.K.; Luo, J.J.; Masson, S.; Jury, M.R.; Rao, S.A. Coupled ocean–atmosphere variability in the tropical Indian Ocean. In *Earth’s Climate: The Ocean–Atmosphere Interaction*; Wang, C., Xie, S.-P., Carton, J.A., Eds.; 2003; pp. 189–212. Available online: [https://ftp.cpc.ncep.noaa.gov/hwang/OLD/Yamagata\\_2004\\_GR.pdf](https://ftp.cpc.ncep.noaa.gov/hwang/OLD/Yamagata_2004_GR.pdf) (accessed on 30 April 2024).
46. Tazalika, L.; Jury, M.R. Spatial and temporal patterns of intra-seasonal rainfall oscillations over tropical Africa: Their evolution and propagation. *Theor. Appl. Climatol.* **2008**, *94*, 67–80. [[CrossRef](#)]
47. Vigaud, N.; Richard, Y.; Rouault, M.; Fauchereau, N. Moisture transport between the south Atlantic Ocean and southern Africa: Relationships with summer rainfall and associated dynamics. *Clim. Dyn.* **2009**, *32*, 113–123. [[CrossRef](#)]
48. Masters, J. Five of Africa’s Top 30 Deadliest Weather Disasters Have Occurred since 2022. 2023. Available online: <https://yaleclimateconnections.org/2023/05/> (accessed on 30 April 2024).
49. Chirps. African Gauge Count. 2023. Available online: <http://data.chc.ucsb.edu/products/CHIRPS-2.0/diagnostics/stations-perMonth-byRegion/pngs/Africa.station.count.CHIRPS-v2.0.png> (accessed on 30 April 2024).

**Disclaimer/Publisher’s Note:** The statements, opinions and data contained in all publications are solely those of the individual author(s) and contributor(s) and not of MDPI and/or the editor(s). MDPI and/or the editor(s) disclaim responsibility for any injury to people or property resulting from any ideas, methods, instructions or products referred to in the content.